

pubs.acs.org/acsapm Article

Effect of Fluorophobic Character upon Switching Nanoparticles in Polymer Films from Aggregated to Dispersed States Using Immersion Annealing

Mengxue Zhang, Taylor Larison, Sidong Tu, Olga Kuksenok, and Morgan Stefik*



Cite This: ACS Appl. Polym. Mater. 2022, 4, 7042–7053



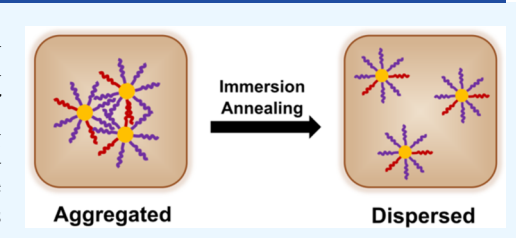
ACCESS I

III Metrics & More

Article Recommendations

Supporting Information

ABSTRACT: For nanoparticle (NP) polymer composites, the state of dispersion vs aggregation significantly affects optical, electronic, thermal, and mechanical properties. The switching of NP distribution states thus far was limited to polymer solutions or bulky polymer-grafted NPs. Herein, for the first time, NP distribution states within polymer films are switched by adjusting fluorophobic interactions and the enthalpy of mixing with immersion annealing. The fluorophobic effect is the tendency of fluorinated molecules to strongly phase-separate from non/less fluorinated molecules. A highly fluorophobic homopolymer, poly(perfluorooctyl



acrylate) (PFOA), was combined with gold NPs of variable fluorophobic character, prepared using mixtures of small-molecule ligands (xF-NP, where x is the mol % fluorinated ligands). Low-to-moderately fluorophobic F-NPs with PFOA were aggregated after spin coating where film swelling via immersion annealing with moderately fluorophobic trifluoro toluene (TFT) generally led to a dispersed state. In contrast, the highly fluorophobic 100F-NPs were dispersed regardless of immersion annealing. This behavior was attributed to the PFOA acting like a surfactant to enable dispersion of highly fluorophobic NPs in TFT. Since these two distinct behaviors favor nonoverlapping ranges of xF-NP compositions, the NPs with intermediate compositions exhibited limited dispersibility. This fluorophobic switchability could enable time- and chemical-selective sensing of fluorinated compounds in the future.

KEYWORDS: nanoparticle, distribution state, switchability, fluorophobic interaction, immersion annealing, kinetical entrapment

1. INTRODUCTION

The combination of nanoparticles (NPs) with polymers has been broadly pursued for enhanced properties that often depend upon the NP distribution state, spanning the continuum from homogeneously dispersed to fully aggregated. 1-4 For example, compared to aggregated nanoparticles, polymer elastomers with homogeneously dispersed NPs have higher elastic modulus, tensile strength, elongation at yield, and compressive moduli. Gas permeability also depends on the NP distribution state where dispersed NPs can disrupt polymer chain packing and increase the gas diffusivity, whereas aggregated NPs are sometimes reported to decrease the gas diffusivity. Similarly, Forster resonance energy transfer (FRET) is sensitively dependent upon the spacing between chromophores with an inverse dependence upon this distance to the sixth power.9 It follows that FRET strength depends sensitively on the spacing between NP donors and NP acceptors. 10 Within these and other contexts, the distribution state of NPs within polymers broadly affects a range of properties.

The equilibrium distribution of NPs within a polymer is determined by the balance of entropic and enthalpic contributions. The dispersion of NPs increases their translational entropy. When NPs become larger than the polymer chain, the stretching of the polymer chain to wrap about the

NP causes a loss of polymer conformational entropy. This effect is avoidable when the NPs are smaller than the polymer chain.¹² The effective interaction parameter, χ , is a largely enthalpic term that relates to the enthalpy of a two-body interface. The interface formation can either release enthalpy (negative χ) or more generally consume enthalpy (positive χ). The balance of these and other thermodynamic driving forces determines the distribution state of NPs within a homopolymer, particularly for NPs with small-molecule ligands. 12-14 In contrast, there are many reports of polymer-grafted NPs distributed within homopolymers; 15-18 however, this manuscript rather focuses on NPs with small-molecule ligands which have a substantially larger volume fraction of the NP core. Thus, the entropy of mixing is often largely determined by the nominal NP size and, for NPs with small-molecule ligands, the enthalpy of mixing is largely dependent upon intermolecular interactions of the ligands with the polymer.

Received: June 7, 2022

Accepted: September 13, 2022 Published: September 22, 2022





It follows that the ability to modulate the dispersed/ aggregated state of NPs within polymers can lead to pronounced changes in the corresponding nanocomposite properties. Switchable distribution states of NPs in solutions have been shown via many modalities of stimuli-sensitive triggers, including electrochemical REDOX, 19 solvent mediation, metal-ion coordination, photoisomerization induced polar interactions,²² and temperature-induced DNA denaturation.²³ While a number of works have examined switchable NP distribution states within polymer solutions²⁴ or using polymer-grafted NPs,²⁵ such switching with small-molecule ligated NPs within polymer films remains understudied. The motion of NPs within a polymer film is naturally challenging owing to the typically high polymer viscosity. NP-polymer films thus present new opportunities by combining facile kinetic control of NP placement when dry with switchable distribution states while swollen with solvent to both increase mobility and modify the intermolecular interactions (γ) .

The fluorophobic effect is a unique intermolecular interaction where fluorinated components robustly phaseseparate from nonfluorinated components as caused by the relatively low surface energy of fluorinated molecules.²⁶ For this reason, the term "fluorophobic" is often preferred to the equivalent term "fluorophilic". A remarkable example demonstrated that two immiscible homopolymers with short fluorinated end groups self-assembled into a lamellar arrangement based on the fluorophobic repulsion of the end groups, leading to pseudo-diblock polymer type behavior. 30 Similarly, the distribution of xF-NPs into a fluorophobic homopolymer was recently shown to depend significantly upon the fluorophobic strength of the NPs where highly fluorophobic NPs were more dispersed.³¹ Fluorophobic intermolecular interactions are thus uniquely strong and are promising candidates to enable switchable NP distribution states by altering the molecular environment within polymer films.

Here, the ability to disperse fluorophobic NPs within a fluoropolymer film is examined using immersion annealing. The results were mapped as a function of fluorophobic interactions and were compared to computer simulations, which agreed qualitatively with experimental observations. The ability to switch the distribution state depended upon modulating the strength of fluorophobic solvent/polymer interactions as well as kinetic entrapment.

2. METHODS

2.1. Materials. Gold trichloride (99.9%, AuCl₃) was purchased from Strem Chemical and stored under argon atmosphere. Didodecyldimethylammonium bromide (98%, DDAB) and tetra-nbutylammonium borohydride (≥98%, TBAB) were purchased from Tokyo Chemical Industry (TCI) America and stored under argon atmosphere. Methyl-2-bromopropionate (97%) and 1H,1H,2H,2Htridecafluoro-n-octyl acrylate (>98%, FOA) were purchased from Tokyo Chemical Industry (TCI) America and stored in a refrigerator. 1H,1H,2H,2H-perfluorooctyl-1-thiol (97%, PFOT) was purchased from Synquest Laboratories and stored under argon atmosphere. Tris[2-(dimethylamino)ethylamine] (99%, Me₆TREN) was purchased from Alfa Aesar and stored under argon atmosphere. Copper(I) bromide (99.99%, Cu(I)Br) and anhydrous cyclohexane were purchased from Sigma-Aldrich and stored under argon atmosphere. Octyltrichlorosilane (97%) was purchased from Acros Organics and stored under argon atmosphere. Dodecylamine (97%, DDA) was purchased from Thermo Scientific Chemicals and stored under argon atmosphere. Basic aluminum oxide and hydrochloric acid (37% solution in water) were purchased from Acros Organics. 1-Dodecanethiol (98%, DDT) was purchased from BeanTown

Chemical (BTC) and stored in a refrigerator. Trifluoro toluene (>99%, TFT), perfluorohexane (\geq 98%, 85% *n*-isomer, C_6F_{14}), and anhydrous iodine lumps (99.99%, under argon) were purchased from BeanTown Chemical (BTC). Chloroform-d (99.8%, CDCl₃) was purchased from Cambridge Isotope Laboratories, Inc. Methanol (99.8%, MeOH), toluene (99.5%), hexane (98.5%), and acetone (99.5%) were purchased from Fisher Chemical. Electrical-insulating-grade mica sheets were purchased from McMaster-Carr. The SnakeSkin Dialysis Tubing with 22 mm \times 35 ft dry diameter, 34 mm dry flat width and 3500 MWCO was Purchased from Thermo Fisher Scientific.

- 2.2. Amine-Stabilized Nanoparticle (Am-NP) Synthesis. Dimethylammonium bromide (98%, DDAB) (1.94 g, 4.2 mmol) and toluene (42 mL) were combined under inert atmosphere to yield a 0.1 M DDAB surfactant solution. An aliquot of this 0.1 M DDAB surfactant solution (28 mL) was used to dissolve AuCl₃ (90 mg, 0.3 mmol) in a 125 mL Erlenmeyer flask, forming the AuCl₃ precursor solution. Separately, 0.1 M DDAB surfactant solution (2 mL) was used to dissolve dodecylamine (97%, DDA) (0.17 g, 0.9 mmol) and then added to the AuCl₃ precursor solution while stirring at 220 rpm, turning the solution color from dark orange to light yellow. In a separate vial, tetra-*n*-butylammonium borohydride (≥98%, TBAB) (300 mg, 1.1 mmol) and 0.1 M DDAB surfactant solution (12 mL) were combined to yield the TBAB reducing agent. Both the AuCl₃ precursor solution and the TBAB reducing agent were moved out of the glovebox. The TBAB reducing agent was then added to the AuCl₃ precursor solution while stirring at 1100 rpm, causing the reaction to become dark purple immediately due to the formation of aminestabilized NPs (Am-NPs).
- 2.3. Mixed-Ligand Fluorophobic Nanoparticle (xF-NPs) Synthesis. Mixed-ligand fluorophobic xF-NPs were prepared by premixing the desired ratio of DDT and PFOT, then injecting the mixture into the Am-NP solution with stirring at 1100 rpm for 15 min. The molar ratio of total thiol/gold was 1:1. The resulting solution was then heated to 120 °C for 20 min to allow ligand displacement. The fluorophobic NPs were named xF-NPs, where x is the composition of the ligands on the NP surface containing *x* mol % of the fluorinated ligand PFOT. The xF-NPs with $x \ge 85$ mol % were termed "highly fluorophobic", 50 < x < 85 were termed "moderately fluorophobic", and $50 \le x$ were termed "low fluorophobic". After ligand exchange, the low-to-moderately xF-NPs were washed using two times with toluene (5 mL) and two times with trifluoro toluene (TFT, 5 mL) with 5 min ultrasonication respectively and then collected in methanol (MeOH, 25 mL) by centrifugation at 8000 rpm for 15 min. Highly fluorophobic α F-NPs were dispersed in a 70/30 vol % TFT/MeOH mixture (5 mL) and collected in cold chloroform (CHCl₃, 25 mL) by centrifugation at 8000 rpm for 15 min. This process was repeated four times to ensure NP cleanness.
- 2.4. ¹H NMR Experiments to Determine xF-NP Ligand Shell Composition. To validate the DDT/PFOT ratio on the xF-NP surface, ¹H NMR experiments were performed. A 5 mg portion of xF-NPs was dispersed using either TFT (0.6 mL) for low-to-moderately fluorophobic NPs or 70/30 vol % TFT/MeOH mixtures (0.6 mL) for highly fluorophobic NPs, followed by 5 min of ultrasonication. In a separate vial, iodine (8 mg, 0.03 mmol) was dissolved in chloroform (0.6 mL). Then, xF-NP solution was combined with the iodine solution, sonicated for 20 min, and was then placed at RT overnight. After this ligand stripping reaction, the black precipitates and iodine were removed by filtration. The resulting disulfide solution had the solvent removed by ambient evaporation and was then dissolved in a TFT/CDCl₃ (0.25 mL/0.45 mL) mixture. Then, this solution underwent 300 MHz ¹H NMR measurement with 1 s relaxation time using 128 scans for improved signal-to-noise ratio.
- **2.5.** Poly(perfluorooctyl acrylate) (PFOA) Synthesis. The 1H,1H,2H,2H-tridecafluoro-*n*-octyl acrylate (>98%, FOA) (12.2 mL, 45.3 mmol) previously passed through the basic alumina column to remove inhibitor was placed into a Schlenk flask. Note: FOA may cause skin, eye, and respiratory irritation. Safe handling practices of FOA and other fluorinated reagents must be carefully considered with adequate personal protective equipment, ventilation, and chemical

waste management. To the flask, methyl-2-bromopropionate (79 μ L, 0.7 mmol) was added. The solution was then subjected to four freeze-pump-thaw cycles to remove oxygen. Then, the sealed reaction solution was transferred into an argon glovebox. A Cu(I)Br stock solution was prepared with the addition of tris[2-(dimethylamino)ethyl]amine (99%, Me₆TREN) (149 µL, 0.56 mmol), Cu(I)Br (80 mg, 0.56 mmol), and toluene (1.0 mL). The Cu(I)Br stock solution (635.2 μ L) was then injected into the FOA solution. The Schlenk flask was sealed, removed from the glovebox, placed in a preheated oil bath at 90 °C, and stirred for 2.8 h. The resulting PFOA solution was cooled to 0 °C, diluted with a 20/80 vol % TFT/chloroform mixture, and placed into a SnakeSkin dialysis bag (3500 MWCO, 22 mm). The dialysis bag was placed into a 250 mL Erlenmeyer flask with 100 mL of TFT and 150 mL of chloroform to remove unreacted FOA monomer and Cu(I)Br. The dialysis procedure was repeated three times for 3, 3, and 12 h, respectively. The resulting PFOA was collected by rotary evaporation. Finally, the PFOA was placed in a vacuum oven at 65 °C overnight to dry. The molar mass of PFOA was analyzed with Bruker Advance III-HD 300 MHz ¹H NMR measurement with 2 s relaxation time and 16 scans by dissolving pure PFOA (5 mg) in a mixture of TFT (0.4 mL) and CDCl₃ (0.6 mL).

2.6. Mica Substrates with Hydrophobic Surface Treatments. Mica substrates were used for spin coating α F-NP/PFOA thin films. The micas were cut into $1 \times 10 \text{ cm}^2$ strips and sonicated within DI water followed by a 20/80 vol % IPA/DI water mixture for 20 min, respectively. The mica strips were cleaned with oxygen plasma for 30 min and transferred into an argon glovebox for a hydrophobic treatment. Here, the mica strips were submerged within a combination of octyltrichlorosilane (1.4 mL) and anhydrous cyclohexane (80 mL). The container was removed from the glovebox covered with a rubber stopper and purged continuously with nitrogen while adding hydrochloride acid (1 mL) with 37% solution in water. The reaction was allowed to progress for 4 h. Finally, the mica strips were taken out and rinsed with toluene, IPA and DI water twice, respectively. All of the mica strips were cut into 1 × 1 cm squares and stored in a box.

2.7. Solution SAXS Measurements. Solution SAXS measurements were characterized using xF-NP solutions. The low-to-moderately fluorophobic xF-NPs were dispersed in TFT, whereas highly fluorophobic xF-NPs were dispersed in TFT/MeOH mixtures, both at a concentration of 5.77 mg/mL. The solutions were sonicated for 15 min, and an aliquot was injected into a fused silica capillary, which was then flame-sealed and secondarily sealed with wax. The solvent composition was varied to assure good xF-NP dispersion based upon the SAXS pattern (form factor observation) for each xF-NP stock solution.

2.8. Radius of Gyration ($R_{\rm g}$) Identification of PFOA Polymer Chains. The radius of gyration ($R_{\rm g}$) of PFOA was determined with Guinier Analysis of SAXS data using 4 mg/mL PFOA in TFT. The SAXS data were measured using a SAXSLab Ganesha at the South Carolina SAXS Collaborative with an X-ray flux of 1.8 million photons per second incident upon the sample and a sample-to-detector distance of 1400 mm. SAXSGUI (v2.23.23) was used for data fitting with $qR_{\rm g} < 1.3$.

2.9. SEM Measurements for xF-NPs. A Zeiss Ultraplus thermal field emission SEM was used to acquire images for xF-NP size distribution using an acceleration voltage of 5 keV and an in-lens secondary electron detector. The SEM sample was prepared by spin-cast xF-NP in TFT at 5.77 mg/mL onto a silicon substrate at 1500 rpm within 30 s. Measurement statistics were acquired using ImageJ software.

2.10. xF-NP/PFOA film Preparation. The xF-NP/PFOA films were prepared using stock solutions. A portion of the xF-NP stock solution containing the desired amount of xF-NP mass was placed into a vial. A desired amount of PFOA was added via a PFOA stock solution in TFT (500 mg/mL). The xF-NP/PFOA mixture solution was then dried in a fume hood overnight. The desired amount of TFT solvent was added to the dried xF-NP/PFOA mixture for the target concentration. Then, xF-NP/PFOA solution was sonicated for 20 min

prior to spin coating. Five loading % were selected for each fluorinated xF-NP composition: 0.22, 0.37 0.52, 0.74, and 0.98 vol %. Here, an example of 0.22 vol % xF-NP loading into 50 mg PFOA quantifies this procedure.

The density of PFOA was assumed to be 1000 mg/mL. Then, the volume of xF-NPs is equal to

$$v_{xF-NP} = \frac{m_{PFOA}}{\rho_{PFOA}} \times \text{vol \% loading} = \frac{50 \text{ mg}}{1000 \text{ mg/mL}} \times 0.22\%$$

$$= 1.1 \times 10^{-4} \text{ mL}$$
(1)

The density of xF-NPs was assumed to be 10 000 mg/mL, then the mass of xF-NPs within corresponding vol % loading could be represented as

$$m_{\rm F-NP} = \rho_{x{\rm F-NP}} \times \nu_{x{\rm F-NP}} = 10\ 000\ {\rm mg/mL} \times 1.1 \times 10^{-4}\ {\rm mL}$$

= 1.1 mg (2)

For xF-NP stock solution with 5.77 mg/1000 μ L concentration, the volume of stock solution with 0.22 vol % loading becomes

$$v_{xF-NP_stock} = \frac{1.1 \text{ mg}}{5.77 \text{ mg}/1000 \,\mu\text{L}} = 190.6 \,\mu\text{L}$$
(3)

In conclusion, the volume of xF-NP stock solution with 5.77 mg/ 1000 μ L concentration loading into 50 mg of PFOA with 0.22 vol % loading is equal to 190.6 μ L. Then, aliquot TFT was added after drying of the xF-NP/PFOA stock solution to form the desired ratio. Then, this xF-NP/PFOA solution with different nanoparticle loading fractions was used to spin-coat onto 1 \times 1 mica substrates at 1500 rpm within 30 s under fast dry air flow.

2.11. Film Thickness by Reflectometry Measurements. A Filmetrics F20 was used to measure film thickness. The sample was prepared by spin-cast xF-NP/PFOA in TFT onto a silicon substrate at 1500 rpm within 30 s. A Si reference wafer was selected for baseline and air as the background.

2.12. Solvent Immersion Annealing Procedure. The *x*F-NP/PFOA thin films that exhibited aggregation by SAXS were annealed through solvent immersion using TFT/MeOH mixtures. Highly fluorophobic F-NP/PFOA thin films were submerged within a 35/65 vol % TFT/MeOH mixtures, whereas 12/88 vol % TFT/MeOH mixtures were used for low-to-moderately fluorophobic F-NP/PFOA films. The immersion annealing time ranged from 0.5 to 24 h. After immersion annealing, the samples were quickly dried and examined by SAXS.

2.13. Small-Angle X-ray Scattering (SAXS) Characterization. The xF-NP/PFOA films were measured using a SAXSLab Ganesha at the South Carolina SAXS Collaborative. The X-ray source was a Xenocs GeniX3D microfocus source generating a 0.154 nm wavelength beam. The 2D scattering patterns were collected via a Pilatus 300K detector (Dectris). The SAXS data were acquired with an X-ray flux of 21.4 million photons per second incident upon the sample and a sample-to-detector distance of 302.1 mm. The National Institute of Standards and Technology (NIST) reference 640c silicon powder was used for q-calibration, in which the peak position was at $2\Theta = 28.44^{\circ}$ (2Θ is the total scattering angle). After immersion annealing, the samples were dried quickly and the distribution state was measured in multiple positions. The distribution states were found to vary with the rate of drying, thus samples with regions consistent with spherical form factor only were termed "dispersed."

2.14. UV–Vis Measurements. A Shimadzu UV-2450 spectrometer was used to measure the optical properties of xF-NP/PFOA films from 400 to 800 nm as a function of the NP distribution state. A square copper mask $(1 \text{ cm} \times 1 \text{ cm})$ was used.

2.15. xF-NP/PFOA Distribution Analysis via Coarse-Grained Simulations. The equilibrium distribution of xF-NP within PFOA polymer film before and after immersion annealing was characterized using dissipative particle dynamic (DPD) approach. $^{32-34}$ DPD is a computationally efficient coarse-grained approach that uses soft repulsion potentials, thereby making larger systems computationally accessible compared to atomistic molecular dynamics simulations.

DPD has been utilized to model a wide variety of complex multicomponent polymer systems, 33 including polymer-nanoparticles systems. $^{35-40}$ Only the main features of the DPD approach are briefly outlined below. The beads in DPD represent groups of atoms; the motion of these beads is governed by Newton's equations of motion. 32 For the nonbonded beads, the pairwise additive force consists of three contributions: purely repulsive conservative force, dissipative force, and random force. The contributions of all forces vanish beyond a cutoff radius, r_c , which introduces an intrinsic model length scale. 32,34 The conservative force in the form of the soft repulsion potential was chosen, which is the most common choice in DPD 32,33

$$\mathbf{F}_{ij}^{C} = \begin{cases} a_{ij} \left(1 - \frac{r_{ij}}{r_{c}} \right) \mathbf{e}_{ij} & (r_{ij} < r_{c}) \\ 0 & (r_{ij} \ge r_{c}) \end{cases}$$
(4)

where a_{ij} is the repulsion coefficient between the beads i and j separated by a distance $r_{ij} = |r_{ij}|$, $r_{ij} = r_i - r_j$, and $e_{ij} = r_{ij}/r_{ij}$. Two remaining contributions to the total force are

$$\mathbf{F}_{ij}^{\mathrm{D}} = -\gamma \omega^{\mathrm{D}}(\mathbf{r}_{ij})(\mathbf{e}_{ij} \cdot \mathbf{v}_{ij})\mathbf{e}_{ij} \tag{5}$$

$$\mathbf{F}_{ij}^{\mathrm{R}} = \sigma \omega^{\mathrm{R}}(r_{ij}) \zeta_{ij} \Delta t^{-1/2} \mathbf{e}_{ij}$$
(6)

where γ and σ are the strengths of the dissipative and random forces, $\mathbf{v}_{ij} = \mathbf{v}_i - \mathbf{v}_j$ is the relative particle velocity, Δt is the simulation time step, and $w^{R}(r_{ij}) = 1 - r_{ij}/r_{c}$ for $r_{ij} < r_{c}$ and zero otherwise, and $w^{D}(r_{ij})$ $= (w^{R}(r_{ii}))^{2}$. The repulsion coefficient a_{ii} in DPD could be related to the Flory–Huggins polymer–solvent interaction parameter, χ_{ii} , as 32 a_{ij} = a_{ii} + 3.27 χ_{ip} where a_{ii} is the repulsion coefficient between the same type of beads. $a_{ii} = 78$ was chosen in reduced DPD units, which is a common choice corresponding to the three water molecules coarsegrained into a single bead. The ζ_{ij} in eq 6 is a symmetric Gaussian distributed random variable with zero mean and unit variance. The dissipative and random forces (eqs 5 and 6) are coupled through the fluctuation-dissipation theorem 32,34 where the used values were derived and justified previously.³³ The bonded beads are connected by harmonic bonds with the interaction potential: $U_{\text{bond}} = K_{\text{b}}(r_{ij} (r_b)^2$, where $(K_b)^2$, where $(K_b)^2$ defines a spring constant and $(R_b)^2$ is an equilibrium bond distance. The modified segmental repulsive potential (mSRP) approach⁴² was utilized to prevent unphysical chain crossing. It is worth noting that the mSRP DPD formulation captures the effects of entanglements in polymer melts.⁴² Within the mSRP formulation, an additional repulsive force $F_{ij}^{SRP} = b(1 - d_{ij}/d_c)e_{ij}^S$ is applied between the centers of the bonds if the distance between these centers, $d_{ij} = 1$ is below the cutoff distance decrease, $d_{ij} = 1$ is below the cutoff distance decrease, $d_{ij} = 1$ is below the cutoff distance decrease $d_{ij} = 1$ is below the cutoff distance decrease $d_{ij} = 1$ is below the cutoff distance decrease $d_{ij} = 1$ is below the cutoff distance decrease $d_{ij} = 1$ is below the cutoff distance decrease $d_{ij} = 1$ is below the cutoff distance decrease $d_{ij} = 1$ is below the cutoff distance decrease $d_{ij} = 1$ is decreased as $d_{ij} = 1$. 500, $r_b = 0.7$, and mSRP parameters as b = 80 and $d_c = 0.8$; these mSRP parameters were previously shown to effectively reduce topology violations. Remaining parameters are chosen as follows: 2 the beads number density is $\rho = 3$, the mass is m = 1, the cutoff radius is $r_c = 1$, and the strengths of the dissipative and random forces are chosen to satisfy fluctuation-dissipation theorem^{32,34} as $\gamma = 4.5$ and $\sigma = 3.0$. The parameters above and all of the simulation values below are provided in reduced DPD units. The above choice of the degree of coarse-graining allows one to relate the reduced dimensionless unit of length in DPD to the dimensional value of length as $r_c \approx 0.65$ nm, and correspondingly to the reduced unit of time as $\tau_0 \approx 88$ ps. The equations of motion are integrated using velocity-Verlet algorithm with a time step of $\Delta t = 0.01\tau_0$. The simulations were carried out using the Large Scale Atomic Molecular Massively Parallel Simulator (LAMMPS) package 44,45 with mSRP code. 42 All visualizations were performed using the Visual Molecular Dynamics (VMD) software.

First, the xF-NP distribution states upon equilibration within the PFOA matrix dependent on the fluorophobic component of nanoparticles were characterized. Each linear PFOA chain was represented by 30 beads and each xF-NP was represented by a single bead so that a relatively large number of nanoparticles can be

introduced. The single-bead representation of functionalized nanoparticles in DPD was previously used to capture the main features of NPs distributions in various polymer matrices observed experimentally. 37,38,47 It is worth noting that depending on the system studied, nanoparticles can be represented within the DPD framework by various numbers of beads 35,36,48,49 or by explicitly introducing grafted ligands of various lengths and chemical nature. 39,40 Herein, the variation in fluorophobic strength of xF-NPs is mimicked phenomenologically via adjusting the repulsion parameter (a_{ij}) between nanoparticles and polymer beads.

The size of the simulation box in the first series of simulations is 40 \times 40 \times 40 reduced DPD units, with periodic boundary conditions imposed in x and y directions and reflective walls imposed in the zdirection. In these series of simulations, the α F-NPs with four volume fractions (0.25, 0.5, 0.75, and 1.0%) were initially randomly distributed within the PFOA melt. For each volume fraction, the repulsion parameter $a_{ij} \equiv a_{\text{FNP-PFOA}}$ was chosen between $a_{ij} = 95$ and $a_{ii} = 120$ (with the step of five, six values of a_{ii} for each nanoparticle fraction) to mimic affinities between the xF-NPs with different fluorophobic character and PFOA polymer matrix. For each set of simulation parameters, four independent simulations were run for 3 × 106 time steps to ensure that the system reached a steady state. The full distribution of NP aggregates was tracked throughout the simulations and each was repeated with four independent runs. These full cluster size distributions were tracked over time evolution, including largest cluster size and NP fraction within clusters, and were also analyzed using ensemble average characteristics (average number of clusters and average aggregation number). The late time distributions of these clusters for all of the above parameter sets were characterized. Two xF-NPs were considered to belong to the same cluster at a given time instant if their centers were within the cutoff distance r_c . The average number of clusters, the aggregation number, and the average size of the largest cluster were calculated using the data from the last 3×10^5 time steps (60 frames for each independent simulation run, four runs for each parameter set). Here, the aggregation number is defined as 52,53

$$N_{\text{agg}} = \sum_{i} n_{i} P_{i} / n_{i} \tag{7}$$

where P_i is the size of the cluster i (number of xF-NPs within this cluster) and n_i is the number of clusters of this size; the summation is taken over all of the clusters.

In the second series of simulations, to introduce solvent beads and simulate the immersion annealing process, the box size in the zdirection was increased from $40 \times 40 \times 40$ to $40 \times 40 \times 80$. The reflective walls in the z-direction were removed and periodic boundary conditions were imposed in x, y, and z directions, the system was equilibrated for 10^4 time steps upon solvent addition prior to the production runs. The simulations of immersion annealing were conducted for the 1.00 vol % of xF-NPs. The repulsion parameters between xF-NPs and methanol, $a_{\rm FNP-methanol}$, as well as PFOA and methanol, $a_{\text{PFOA-methanol}}$ were chosen as 130, while the repulsion coefficients between TFT and PFOA, $a_{\text{FNP-TFT}}$, as well as TFT and methanol, $a_{\text{TFT-methanol}}$, were chosen as 78 (Table S2). The repulsion coefficients between xF-NPs and PFOA were kept as chosen in the above simulations. The solubility difference was modified by varying the repulsion parameter between xF-NPs and TFT. The solvent phase consists of 35/65 vol % TFT/MeOH beads, similar to that in experiments. The total fraction of solvent beads constitutes 50% of the simulation box. For each set of simulation parameters, four independent simulations were run for 3×10^6 time steps to ensure that the system is equilibrated. The last 3×10^5 time steps were chosen (60 frames for each independent simulation run, four runs for each parameter set) to calculate the number of clusters, aggregation number, and fraction of xF-NPs within large clusters.

3. RESULTS AND DISCUSSION

Switching distribution states of NPs within polymer films via external stimuli have implications for a wide range of applications that alter physical properties. While there are many demonstrations of switchable NP distribution states within solutions or suspensions, $^{54-56}$ the switching of NP distribution states within polymer films remains underexplored. The high viscosity of typical polymer films often impedes such switching which naturally enables one to preserve nonequilibrium distribution states. Immersion annealing is an appealing strategy to increase NP mobility within polymer films while at the same time temporarily modifying the intermolecular interactions (enthalpy of mixing) that determine the equilibrium distribution state. With the enthalpy of mixing often being endothermic (favoring phase separation), the magnitude of this enthalpy can regulate whether the dispersed or aggregated state is preferred by overall free-energy minimization. Several criteria stand out as necessary for switchability: (1) The NPs should be sufficiently stable for distribution state switching. (2) The NP radii should be similar to or smaller than the radius of gyration of the polymer such that NP mixing does not cause excessive loss of conformational entropy. (3) The enthalpy of NP mixing must be adjustable by the uptake of solvent molecules into the polymer film. (4) Similarly, the immersion annealing conditions must be carefully balanced to alter the NP distribution. (5) The immersion annealing solvent mixture should also be easy to remove (high vapor pressure, low boiling point) to enable kinetic entrapment of the annealed NP distribution state.

To compare the effects of NP intermolecular interactions, comparisons should ideally be carried out with identical NP sizes for criteria (1) and (2). Here, a ligand displacement strategy was chosen to decouple NP size effects from subsequent deliberate changes to the ligand chemistry. Turthermore, NP stability is important to consider where thiols were chosen as a sufficiently strong binding group while also being able to displace weakly bound amine ligands from the initial synthesis step. The existence of mixed thiol ligand could avoid the gold core size change and form a mixed monolayer, which could thereby ensure NP stability throughout the immersion annealing process (from 0.5 to 24 h).

The adjustment of NP mixing enthalpy could be achieved via designing the immersion annealing medium to swell but not dissolve, polymer films for criteria (3). S8,59 Most polymers are soluble within a range of solvents which may be suitable for immersion annealing if sufficient poor solvent is included to avoid dissolution of the polymer film. Here, the use of a perfluorinated PFOA polymer film offers a distinct advantage of being robustly insoluble in a wide range of poor solvents. Depending on the step under consideration, the enthalpy of polymer/NP mixing is influenced by the effective interaction parameter either by $\chi_{\rm NP/polymer}$ or $\chi_{\rm NP/swollen-polymer}$. Judicious experimental design enables the latter term to be adjusted by altering the composition of the immersion medium via solvent mixtures.

For criteria (4), if NP dispersion is desired then the immersion medium should reduce the enthalpy of mixing by reducing the mismatch of intermolecular interaction strength between the NP and the swollen polymer (decrease $\chi_{\text{NP/swollen-polymer}}$). At the same time, the immersion medium should not remove the NPs from the polymer film via dissolution. Thus, the inclusion of poor solvents for the NPs is also crucial to maintain sufficiently high interaction strength between the NP and immersion medium, $\chi_{\text{NP/immersion-medium}}$. Hildebrand solubility parameters can be insightful here to estimate these two χ 's based on the differences in Hildebrand space. The typical approximation $\chi_{12} = v_1(\delta_1 - \delta_2)^2/\text{RT}$

assumes a general endothermic enthalpy of mixing. 60,61 It follows that swelling the polymer film with a solvent that reduces the separation in Hildebrand space could promote NP dispersion. Here the use of fluorophobic NP ligands offers an advantage as these NPs are insoluble in a wide range of solvents which helps to avoid NP dissolution into the immersion medium. The selection of trifluoro toluene (TFT) is ideal as a partially fluorophobic solvent that is good for many xF-NPs with varied x mol % fluorinated ligands and is also a good solvent for PFOA, where TFT is also miscible with many poor solvents for the nonfluorinated species such as hexane and methanol.

Finally for criteria (5), the selection of TFT/MeOH and TFT/hexane mixtures has low enough boiling points for rapid evaporation. Thus, a range of processing considerations must be satisfied for the intended switching of NP distribution states with polymer films.

3.1. Synthesis of Mixed-Ligand Fluorophobic Nanoparticles (xF-NPs) and Homopolymer (PFOA). To study the effect of fluorophobic NP character, a series of NPs were prepared with a range of fluorophobic/lipophilic content. In brief, gold NPs were synthesized with aminated ligands that were subsequently displaced using an exchange solution with mixtures of stronger binding thiol ligands (Figure 1a). 62,63 The two ligands used were 1-dodecanethiol (DDT) and H,1H,2H,2H-perfluorooctyl-1-thiol (PFOT) for the lipophilic and fluorophobic ligands, respectively. This combination of different ligand mixtures resulted in NPs with varied fluorophobic character as indicated by the x mol % of PFOT (xF-NP) on the surface of NPs. For example, NPs with 70 mol % PFOT and 30 mol % DDT would be termed 70F-NP. The DDT to PFOT ligand ratio on NPs was quantified via ¹H NMR measurements after iodine ligand stripping (Figure 1b) where the ligand mixture on the NPs closely matched that of the ligand exchange solution with a Pearson's correlation coefficient of $R^2 = 0.9923$ (Figure 1c). The wide range of xF-NPs synthesized led to wide variations in the NP solubility (Table 1). Most xF-NPs (x = 6-62) were soluble in pure TFT; however, highly fluorophobic xF-NPs (x = 88-100) required the addition of a polar solvent such as MeOH (Table 1). Molecules containing CH₂-CF₂ dipoles were previously noted to dissolve better with a minor polar component.⁶⁴ Several solvent mixture solubility isopleths are shown for 97F-NPs in Figure S1, again showing that polar contributions were needed for dispersion of highly fluorophobic F-NPs. The overall solubility trends were consistent with expectations from Hildebrand solubility parameters where DDT-rich NPs were miscible with toluene and PFOT-rich NPs were miscible in highly fluorophobic mixtures with some polar contributions.

A highly fluorophobic polymer, poly(perfluorooctyl acrylate) (PFOA), was selected based on the similar side chain structure as the PFOT ligand and solubility in TFT. PFOA was synthesized via ATRP (Figure 2). The conversion during the PFOA polymerization was analyzed using ¹H NMR, where the reaction was stopped at 86% conversion. The PFOA molecular molar mass was characterized by end group analysis via ¹H NMR, indicating 23 kg/mol.

The conformational entropy loss was considered by the comparison between xF-NP size and PFOA radius of gyration. The NP sizes were measured by analysis of SAXS data. The xF-NPs were either dispersed in pure TFT for x = 6-62 or TFT/MeOH (70/30 vol %) for x = 88-100. The SAXS patterns measured from these samples were fitted using a polydisperse

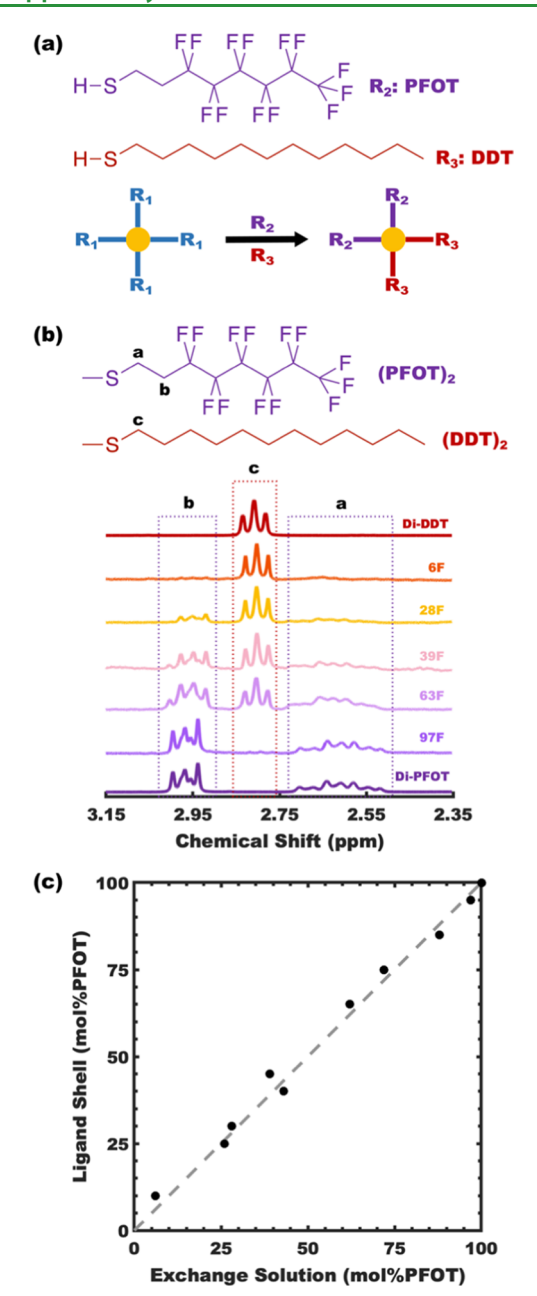


Figure 1. (a) xF-NPs were synthesized starting from NPs with amine ligands, followed by ligand displacement with a mixture of thiols. (b) A series of ${}^{1}H$ NMR measurements were used to determine the ligand mixture composition of xF-NPs after a ligand stripping reaction that produced the corresponding di-sulfides. (c) The ligand mixture composition in the exchange solution closely matched the resulting mixed-ligand shell composition of xF-NPs (mol % PFOT).

spherical form factor model to derive an average NP diameter of 3.1 \pm 0.5 nm (Table S1). Also, analysis of sample 62F-NP by SEM identified an average ~3.1 nm diameter that was consistent with the SAXS form factor interpretation of 3.21 nm (Figure S5). The PFOA radius of gyration ($R_{\rm g}$) was determined to be 2.8 nm using Guinier Analysis of solution SAXS data (Figure S2). This value is significantly greater than the radius of xF-NPs, indicating the contribution from entropy could be neglected. Thus, a fluorinated homopolymer and a series of tailored xF-NPs were prepared for the study of switchable NP distribution states.

3.2. SAXS Characterization of xF-NP/PFOA Distribution State. SAXS measurements allowed facile interpretation of the xF-NP/PFOA distribution states both as spin-coated and after immersion annealing. All compositions of xF-NPs with a range of NP loadings (vol % NP in PFOA) were examined. Films were spin-coated from pure TFT due to the selective solubility of PFOA. The film thicknesses were ~ 75 nm (Figure S3). SAXS measurements were taken at multiple positions of each sample to assign a binary label of dispersed or aggregated. Since all xF-NP loading fractions were <1 vol %, well-dispersed NPs are expected to yield the classic spherical form factor, analogous to that of dilute NPs dispersed in a solvent. As an example of dispersion, compare the SAXS patterns of 100F-NPs dispersed in TFT/MeOH to that of the 100F-NP/PFOA film (Figure 3a). In contrast, aggregated NPs have a prominent structure factor peak corresponding to the packing of NPs, analogous to that of a pure-NP film. As an example of such aggregation, compare the SAXS patterns of a film of pure 97F-NPs to that of a 97F-NP/PFOA film (Figure 3b). The example structure factor peak at $q = 1.4 \text{ nm}^{-1}$ ($d = 1.4 \text{ m}^{-1}$) $2\pi/q = 4.49$ nm) approximately corresponds to the center-tocenter NP distance for randomly packed spheres. 65 The SAXS d-spacing of 4.49 nm corresponds to the nearest neighbor spacing that includes the ligand shell. Such close spacings indicate minimal PFOA between the aggregated xF-NPs. For clarity, an example form factor and structure factor are shown (Figure S4) where their product corresponds to the observed scattered intensity. For dispersed and dilute NPs, the structure factor is equal to 1 so the scattering pattern corresponds to the form factor alone. This method was applied to interpret the distribution state for all samples at each stage as summarized in Figure 4.

3.3. Behavior of xF-NP/PFOA Film As Spin-Coated and after Immersion Annealing. The NP/polymer distribution states were checked by SAXS both as spin-coated (Figure 4a) and after immersion annealing (Figure 4b). These as spin-cast trends are similar but different from those previously reported³¹ and were possibly associated with the changes to the NP synthesis and purification procedures (size, dispersity, ligand shell density), the PFOA synthesis (molecular weight, viscosity), or the spin coating conditions (rpm, gas flow rates). Overall, the ability of the NPs to switch between dispersed and aggregated states was observed to progress through two distinct fluorophobic-based mechanisms; the lowto-moderately fluorophobic F-NP distribution trends were consistent with enthalpy of mixing considerations, whereas highly fluorophobic F-NP distribution trends were consistent with PFOA behaving as a compatibilizer/surfactant. These mechanism trends are next elaborated separately.

The low-to-moderately fluorophobic xF-NPs (x = 6-62) universally exhibited aggregation in PFOA as spin-coated (Figure 4a). The significant DDT ligand fraction in these NPs is expected to increase the $\chi_{F\text{-NP/PFOA}}$ since DDT is lipophilic while PFOA and PFOT are highly fluorophobic. In other words, the fluorophobic NP and PFOA strengths were poorly matched, leading to NP aggregation. This aggregation as a result of fluorination extent is a hallmark of fluorophobic behavior. To lower χ , these composites were subjected to immersion annealing for 0.5–7.5 h with 12 vol % TFT in MeOH to swell the PFOA without dissolving either the NPs of the PFOA (Table 1). All of the low-to-moderately fluorophobic NPs (6–62)F-NPs are miscible in pure TFT as validated separately with SAXS (Figure 4c), thus establishing

Table 1. List of Good and Poor Solvents for xF-NPs and PFOA as well as Immersion Annealing Conditions

		good solvent	poor solvent	immersion annealing
highly fluorophobic	PFOA	pure TFT	pure hexane; pure MeOH	
	100F-NPs	TFT and MeOH (30 vol % of MeOH)	pure TFT; pure toluene; pure hexane; pure C_6H_{14}	TFT/MeOH (35 vol % TFT and 65 vol % MeOH)
	97F-NPs	TFT and MeOH (25–60 vol % of MeOH)	pure TFT; pure toluene; pure hexane; pure C_6H_{14}	
			TFT and C ₆ H ₁₄ ; TFT and hexane	
	88F-NPs	TFT and MeOH (30 vol % of MeOH)	pure TFT; pure toluene; pure hexane; pure C_6H_{14}	
moderately fluorophobic	62F-NPs	pure TFT; pure toluene	pure MeOH	TFT/MeOH (12 vol % TFT and 88 vol % MeOH)
low fluorophobic	6F, 28F and 39F-NPs	pure TFT; pure toluene	pure MeOH	TFT/MeOH (12 vol % TFT and 88 vol % MeOH)

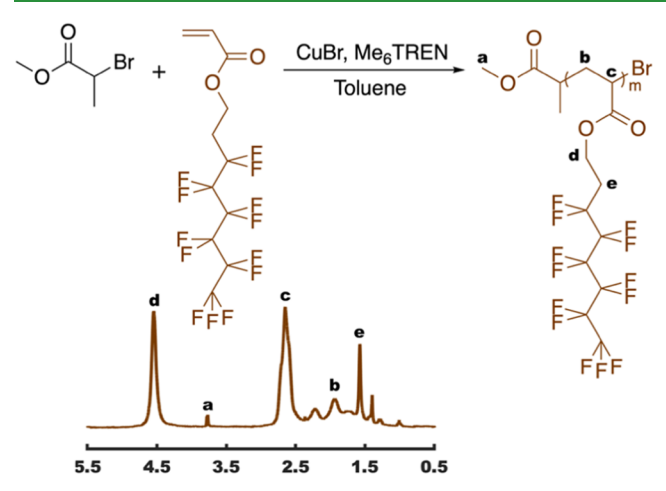
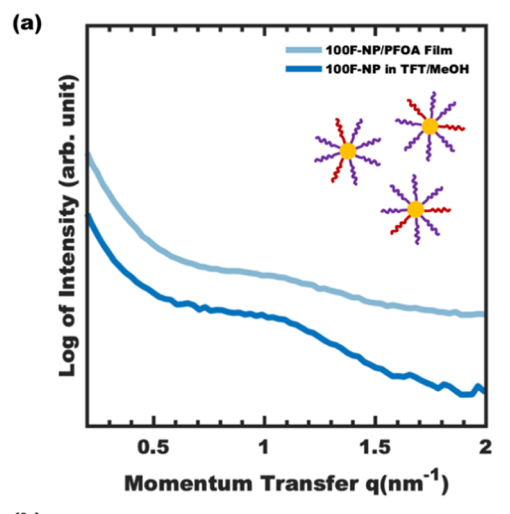


Figure 2. PFOA homopolymer synthesis via ATRP (top) was characterized using ¹H NMR spectroscopy (bottom).

the expectations for immersion annealing with TFT. For all low-to-moderately fluorophobic NP composites (except 39F-NP discussed later), immersion annealing resulted in NP dispersion (Figures 4b and S8). Note that the observation of such form factor patterns is not feasible with surface aggregation of NPs (see the Supporting Information discussion). Here, the relevant χ term is $\chi_{\text{FNP/swollen-PFOA}}$ since the TFT swells the PFOA and modifies its average strength of intermolecular interactions. Again, since TFT is a good solvent for these NPs, swelling PFOA with TFT is expected to reduce the enthalpy of mixing and promote NP dispersion. Samples were rapidly dried after immersion annealing to preserve the annealed distribution states. The $\chi_{\text{FNP/swollen-PFOA}}$ is also dependent on the xF-NP composition where the ability to disperse NPs with TFT reduced with increasing fluorophobic character, (62F- and 88F-NPs). A set of analogous experiments were carried out with immersion annealing in TFT/hexane mixtures (Figure S6) that led to largely similar results with a little more NP aggregation. Similar behaviors were also found by rapidly drying spin-coated samples with air (Figure S7). These different results from spin coating highlight how crucial the drying rate is to control the NP distribution state. To the best of our knowledge, these are the first examples of switching NP distribution states within a polymer film.

The highly fluorophobic F-NP/PFOA composite behaviors were rather consistent with a distinct mechanism (97F- and 100F-NPs). The highly fluorophobic NPs are not soluble in TFT, leading to both visual precipitation and NP aggregation in solution that is detectable with SAXS (Figure 5 and Table



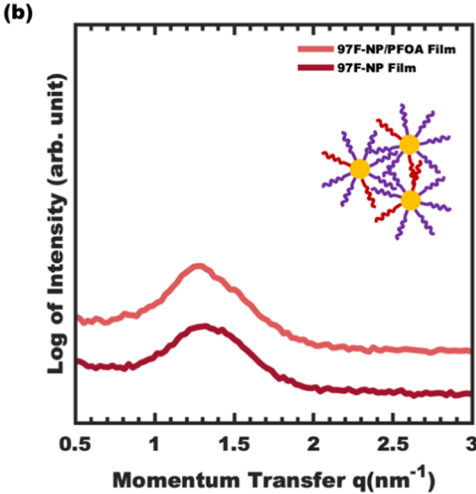
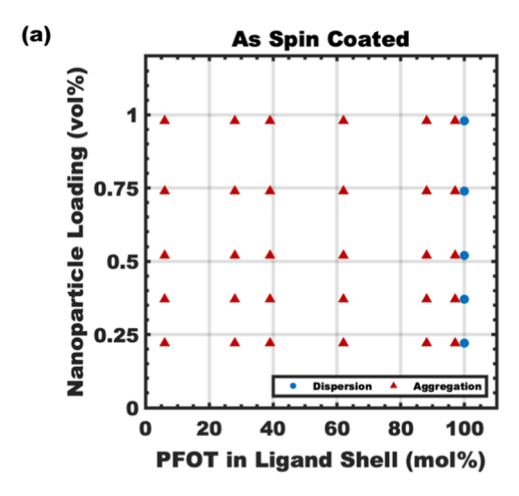
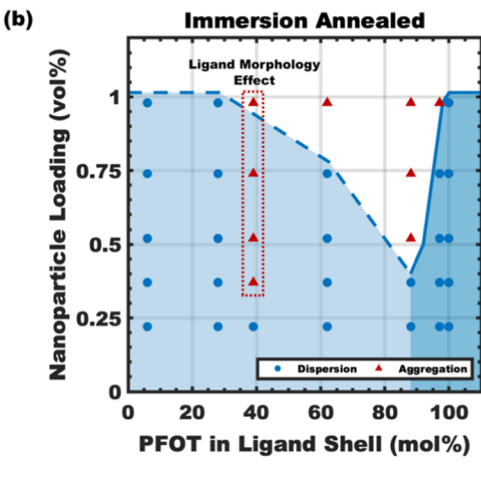


Figure 3. SAXS was used to infer the NP distribution states as being dispersed vs aggregated within PFOA films. (a) SAXS patterns consistent with spherical form factor alone suggest dispersed NPs within PFOA (light blue), analogous to NP dispersions in solvent (dark blue). (b) In contrast, SAXS patterns consistent with additional structure factor suggest aggregation of NPs within PFOA (light red), analogous to the NP–NP correlations found in a pure film of NPs (dark red).

1). Remarkably, the addition of PFOA enables dispersion of these highly fluorophobic F-NPs (Figure 5). This change in NP dispersability is consistent with PFOA behaving as a fluorophobic compatibilizer/surfactant to minimize direct TFT-NP interactions in favor of NP-PFOA separation and PFOA-TFT interactions (Figure 6). This remarkable solution





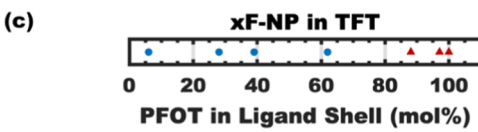


Figure 4. Distribution state data for α F-NP/PFOA thin films were mapped both (a) as spin-coated and (b) after immersion annealing. Five α F-NP loading % into PFOA were selected for each fluorinated composition: 0.22, 0.37, 0.52, 0.74 and 0.98 vol %. The immersion annealing behavior was compared to (c) NP solubility in pure TFT solvent. The shaded regions in (b) correspond to suggested dispersion mechanisms, including reduced enthalpy of mixing via TFT-uptake (light blue) and reduced enthalpy of mixing via PFOA-surfactant behavior (dark blue).

behavior explains the unique dispersion of 100F-NP/PFOA composites as spin-coated. Furthermore, SAXS measurements on 100F-NP/PFOA taken during and after immersion annealing also indicated dispersion (Figures 5 and S8). The aggregation of closely related 97F-NP/PFOA composites as spin-coated was presumably driven by the presence of DDT ligands that were repelled by the fluorophobic PFOA where immersion annealing evidently mitigated this repulsion and enabled dispersion (Figure 4).

Two xF-NP compositions warrant further explanation. The 88F-NPs inability to disperse during immersion annealing was attributed to it being too fluorophobic for the first mechanism (Table 1) and not fluorophobic enough for the second mechanism (Figure 4b, shaded areas). The aggregation of 39F-NP/PFOA composites after immersion annealing indicated an

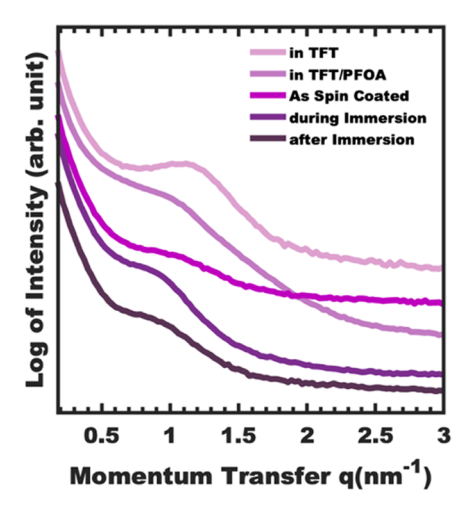


Figure 5. SAXS data (from top to bottom) of 100F-NPs in TFT, 100F-NPs in \sim 30/70 vol % PFOA/TFT, 0.98 vol % 100F-NPs in PFOA as spin-coated, the same film measured in situ during immersion annealing, and finally the same after immersion annealing.

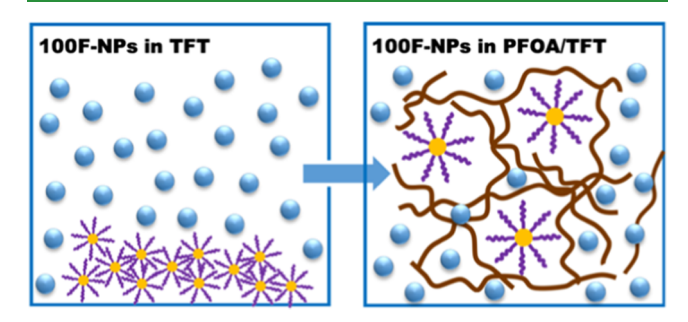


Figure 6. Depiction of the PFOA-surfactant behavior that explains how 100F-NPs are insoluble in pure TFT (left) but are dispersible via a surfactant effect when PFOA is added (brown line).

unexpectedly high $\chi_{39\text{F-NP/swollen-PFOA}}$ that was reproduced with multiple NP batches of repeated experiments. Mixed-ligand NPs have shown many such deviations from the expectations of continuum thermodynamics in the past that were attributed to nonrandom ligand morphologies leading to cavitation or confinement effects. 63,66,67

3.4. Optical Changes with xF-NP/PFOA Distribution State. Gold NPs are widely used in biosensors, biomedical diagnosis, as well as catalysis, where the corresponding properties dependent on the size and distribution state. For example, optical redshifts of the absorption band can be caused by surface plasmon resonance changing with increasing NP size. The optical trends for 0.98% 28F/PFOA followed such a trend where the initially aggregated NPs exhibited an absorption peak of 558 nm, whereas the dispersed distribution after immersion annealing exhibited an absorption peak of 544 nm (Figure S10). Such a shift in optical properties could be used as a detector to identify exposure to fluorinated compounds. It is noted that complex phenomena in NP optical responses have been discussed elsewhere where changes to local polarity, drying processing, NP loading fraction, or fluorinated ligand composition can result in red/ blueshifts depending on the details of the interaction.⁶ Regardless of possible complexity in the optical response, shifts in peak absorption remain relatively simple to detect and make these switchable NPs of interest for future sensing applications for fluorinated compounds.

3.5. Coarse-Grained Simulations of xF-NP/PFOA Initial Distribution State. Dissipative Particle Dynamics $(DPD)^{32-34}$ simulations were used to predict equilibrium xF-NP/PFOA distribution states and immersion annealing behaviors. The distribution states were calculated based on the repulsion coefficient between beads i and j, a_{ij} . For example, a_{ij} values of 95 and 105 correspond to dispersion and aggregation, respectively (Figure 7a-c). The cluster size

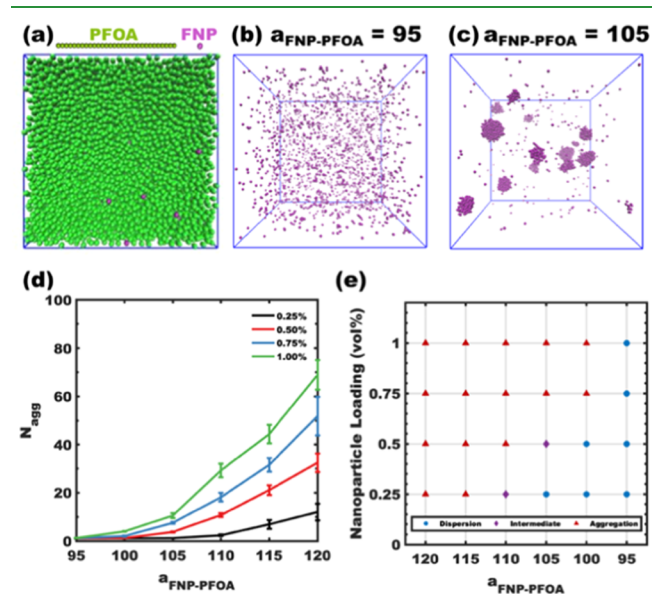


Figure 7. Computer simulations of the NP distribution states in pure PFOA as a function of NP loading fraction and interaction strengths (a_{ij}) . (a) Snapshot of an initial PFOA (green) and xF-NP (purple) distribution. (b, c) Simulations snapshots upon equilibration for films with $a_{ij} = 95$ in (b) and $a_{ij} = 105$ in (c), all with 1.00 vol % NPs. For clarity, only the NPs are shown. (d) The cluster aggregation number (eq 7) increases with a_{ij} . Aggregation statistics were derived from four simulated iterations using the last 3×10^5 steps. (e) NP distribution states for various loading fractions and interaction strengths.

distributions corresponding to the simulation snapshots in Figure 7b,c are also shown in Figure S11. Here, an increase in a_{ii} corresponds to decreasing x in xF-NP. To quantitatively distinguish the distribution state (dispersion, partial aggregation and aggregation), the fractions of the xF-NPs that belong to the relatively large clusters with respect to the total number of NPs were calculated. To filter out the short-lived small clusters, only clusters that contain more than 13 xF-NPs were considered (this value is defined by the coordination number in DPD simulations). Since simulations included the complete xF-NP positional data, the distribution states were labeled with additional granularity including "partially aggregated." In contrast, experimental xF-NP distribution states were labeled in a binary manner. In detail, if the fraction of xF-NPs within these clusters remained close to zero (<0.1), the nanoparticles were considered dispersed, whereas if the fraction of xF-NPswithin these clusters exceeded 0.8, the NP dispersion state was defined as aggregation. For all of the intermediate scenarios in which the fraction of the nanoparticles within the relatively large clusters was equal to or lower than 0.8 but higher than 0.1, the particles were considered to be partially aggregated.

The aggregation process was tracked based on the average number of clusters, the average size of the largest cluster, the average aggregation number, and the fraction of NPs that belong to relatively large clusters as defined above (Figures 7d, S12, and S13). A summary map of computational distribution states is shown in Figure 7e where dispersion/aggregation was determined based on NP aggregation number (Figure 7d) and the fraction of particles within the relatively large clusters (Figure S12b) as defined above. Neither changing the simulation box size (Figures 7d and S14a,b) nor minor changes to the aggregation threshold (Figure S14c,d) markedly affected these conclusions. Similar to the spin-coated results (Figure 4a), these simulations were consistent with the enthalpy of mixing $(\chi_{\text{FNP/PFOA}})$ determining the distribution state. We note that our simulation approach using a single bead per NP only accounts for variation in xF-NP/PFOA phenomenologically, thereby mimicking the degree of fluorophobic repulsion between PFOA and PFOT without directly accounting for the possible effects of the ligands morphology. Hence, while the trends in simulations generally correspond to those in experiments, the observed differences may be attributed to the simplified representation of NPs and to the fact that the simulation results correspond to the wellequilibrated states without accounting for any possible effects of kinetic trapping during spin casting.

3.6. Coarse-Grained Simulations of xF-NP/PFOA after Immersion Annealing. DPD was also used to simulate the immersion annealing process by increasing the box size to include solvent beads for good solvent (TFT) and poor solvent (MeOH) (Figure 8a,b). Two cases with varied fluorophobic character were considered: case I (highly fluorophobic 100F-NPs, $a_{\text{FNP-PFOA}} = 95$, $a_{\text{FNP-TFT}} = 110$) and case II (low-to-moderately fluorophobic F-NPs, $a_{\text{FNP-PFOA}} = 110$, $a_{\text{FNP-TFT}} = 80$). The values of a_{ij} were chosen to mimic measured solubility trends for each pair (Table 1). With the addition of solvent beads, the swelling of the PFOA films (Figure S15) was

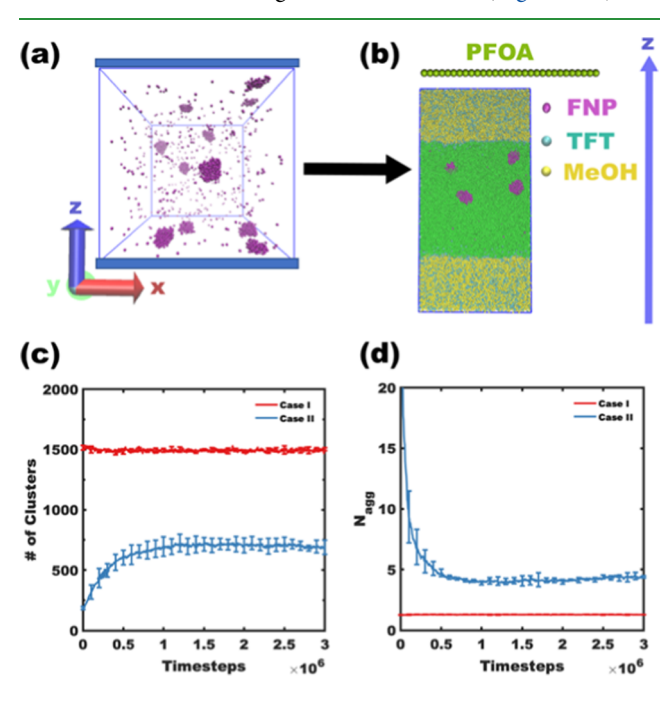


Figure 8. Simulations of immersion annealing where (a) NP/PFOA is (b) combined with a majority of nonsolvent (yellow beads represent MeOH) and a minority of good solvent (indigo beads represent TFT) with periodic boundaries. (c) Time evolution of the number of clusters and (d) the corresponding aggregation numbers are shown for both cases.

observed. The MeOH beads did not diffuse into the film (Figure S16c,d), while the TFT beads were dispersed within the PFOA film causing its swelling (Figure S16a,b). The late time snapshots for cases I and II are shown in Figure S17a,b, indicating dispersion and aggregation, respectively. Here case I demonstrates that low repulsion (low χ) enables dispersion in equilibrium and during immersion annealing. In contrast, case II computationally demonstrates distribution state switching where dispersion is enabled by solvent swelling to reduce the enthalpy of mixing (Figure 8c,d). Note the simulation approach could phenomenologically validate two extreme distribution states (dispersion/aggregation) of xF-NP within PFOA thin film observed from the experiments by adjusting the degree of fluorophobic repulsion, without directly accounting for the possible effects of ligand morphology. Thus, the computational immersion annealing trends were consistent with experimental observations and the postulated mechanisms.

4. CONCLUSIONS

This work demonstrates the first switchability of NP distribution states within a polymer film (PFOA) by adjusting fluorophobic interactions. Judicious experimental designs including criteria 1-5 were elaborated and demonstrated. A ligand exchange strategy for xF-NPs enabled comparisons with similar average NP diameters while having sufficient NP stability. This work showed that NP distribution states are switchable when initially aggregated NP/PFOA films are immersion annealed using good solvents for the xF-NP (low $\chi_{\rm NP/immersion-medium}$) via reduction of the enthalpy of mixing. Related spin coating experiments revealed that both the equilibrium NP dispersion state from solution and the equilibrium NP aggregation state in pure PFOA were accessible depending on the solvent removal rate. A separate compatibilization/surfactant effect was noted that enabled 100F-NP/PFOA to yield dispersions regardless of 100F-NP being insoluble in pure TFT. The complexity of mixed-ligand NPs was also highlighted by 39F-NPs, which deviated from the expectations of continuum thermodynamics and was attributed to a change in ligand morphology. DPD simulations predicted equilibrium distribution states as well as general immersion annealing behaviors, both of which were consistent with the general experimental observations. These results suggest that similar materials could enable time-dependent chemical sensing of fluorinated compounds in the future.

ASSOCIATED CONTENT

Supporting Information

The Supporting Information is available free of charge at https://pubs.acs.org/doi/10.1021/acsapm.2c00968.

97F-NP solubility plot; estimation of radius of gyration of PFOA polymer chains; reflectometry measurement of film thickness; fitting for form factor, structure factor, and complete model; SEM for xF-NP size identification; solvent effect on immersion annealing; illustration of dry rate effect on NP distribution; SAXS patterns for xF-NP/PFOA in TFT, TFT/PFOA solution, as spin-cast film, and after immersion annealing with varied F-NP vol % loading; consideration of NP distribution on film surface; optical property changes before/after immersion annealing measured by UV—vis spectroscopy; computational simulations of the cluster distribution for 1 vol %

 α F-NPs within PFOA; α F-NP distribution in pure PFOA; simulation results for timed evolved; box size depended number of clusters and aggregation numbers; fraction of beads within the clusters of size larger than 10 for each volume fraction of F-NPs; normalized total number of F-NPs of the size of the largest cluster; snapshots of PFOA distribution upon solvent addition; cases after immersion annealing; NP diameter based on SAXS data fitting by polydisperse hard sphere form factor model; and selection of soft repulsion parameter for immersion annealing simulation (PDF)

AUTHOR INFORMATION

Corresponding Author

Morgan Stefik – Department of Chemistry and Biochemistry, University of South Carolina, Columbia, South Carolina 29208, United States; ⊙ orcid.org/0000-0002-2645-7442; Email: morgan@stefikgroup.com

Authors

Mengxue Zhang — Department of Chemistry and Biochemistry, University of South Carolina, Columbia, South Carolina 29208, United States

Taylor Larison – Department of Chemistry and Biochemistry, University of South Carolina, Columbia, South Carolina 29208, United States; ⊚ orcid.org/0000-0002-4418-9330

Sidong Tu — Department of Materials Science and Engineering, Clemson University, Clemson, South Carolina 29634, United States

Olga Kuksenok – Department of Materials Science and Engineering, Clemson University, Clemson, South Carolina 29634, United States; orcid.org/0000-0002-1895-5206

Complete contact information is available at: https://pubs.acs.org/10.1021/acsapm.2c00968

Author Contributions

The manuscript was written through contributions of all authors. All authors have given approval to the final version of the manuscript.

Notes

The authors declare no competing financial interest.

ACKNOWLEDGMENTS

M.Z., S.T., and M.S. were supported by the South Carolina EPSCoR GEAR Program under Award #20-GE02. T.L. was supported by the National Science Foundation EPSCoR Program under NSF Award #OIA-1655740. This work made use of the South Carolina SAXS Collaborative. Clemson University is acknowledged for the generous allotment of computation time on Palmetto cluster. Sean Wechsler is thanked for assistance with SEM measurements.

REFERENCES

- (1) Ghosh, S. K.; Pal, T. Interparticle Coupling Effect on the Surface Plasmon Resonance of Gold Nanoparticles: From Theory to Applications. *Chem. Rev.* **2007**, *107*, 4797–4862.
- (2) Vaia, R. A.; Maguire, J. F. Polymer Nanocomposites with Prescribed Morphology: Going beyond Nanoparticle-Filled Polymers. *Chem. Mater.* **2007**, *19*, 2736–2751.
- (3) Suttiponparnit, K.; Jiang, J.; Sahu, M.; Suvachittanont, S.; Charinpanitkul, T.; Biswas, P. Role of Surface Area, Primary Particle Size, and Crystal Phase on Titanium Dioxide Nanoparticle Dispersion Properties. *Nanoscale Res. Lett.* **2011**, *6*, 27.

- (4) Pandey, Y. N.; Papakonstantopoulos, G. J.; Doxastakis, M. Polymer/Nanoparticle Interactions: Bridging the Gap. *Macromolecules* **2013**, *46*, 5097–5106.
- (5) Liu, H.; Webster, T. J. Mechanical properties of dispersed ceramic nanoparticles in polymer composites for orthopedic applications. *Int. J. Nanomed.* **2010**, *5*, 299–313.
- (6) Merkel, T. C.; Freeman, B. D.; Spontak, R. J.; He, Z.; Pinnau, I.; Meakin, P.; Hill, A. J. Ultrapermeable, Reverse-Selective Nanocomposite Membranes. *Science* **2002**, *296*, 519.
- (7) Matteucci, S.; Raharjo, R. D.; Kusuma, V. A.; Swinnea, S.; Freeman, B. D. Gas Permeability, Solubility, and Diffusion Coefficients in 1,2-Polybutadiene Containing Magnesium Oxide. *Macromolecules* **2008**, *41*, 2144–2156.
- (8) Su, N. C.; Smith, Z. P.; Freeman, B. D.; Urban, J. J. Size-Dependent Permeability Deviations from Maxwell's Model in Hybrid Cross-Linked Poly(ethylene glycol)/Silica Nanoparticle Membranes. *Chem. Mater.* **2015**, 27, 2421–2429.
- (9) Förster, T. Zwischenmolekulare Energiewanderung und Fluoreszenz. *Ann. Phys.* **1948**, 437, 55–75.
- (10) Shi, J.; Tian, F.; Lyu, J.; Yang, M. Nanoparticle based fluorescence resonance energy transfer (FRET) for biosensing applications. *J. Mater. Chem. B* **2015**, *3*, 6989–7005.
- (11) Thompson, R. B.; Ginzburg, V. V.; Matsen, M. W.; Balazs, A. C. Predicting the Mesophases of Copolymer-Nanoparticle Composites. *Science* **2001**, 292, 2469–2472.
- (12) Mackay, M. E.; Tuteja, A.; Duxbury, P. M.; Hawker, C. J.; Van Horn, B.; Guan, Z.; Chen, G.; Krishnan, R. S. General Strategies for Nanoparticle Dispersion. *Science* **2006**, *311*, 1740.
- (13) Thompson, R. B.; Ginzburg, V. V.; Matsen, M. W.; Balazs, A. C. Predicting the Mesophases of Copolymer-Nanoparticle Composites. *Science* **2001**, 292, 2469.
- (14) Lin, Y.; Böker, A.; He, J.; Sill, K.; Xiang, H.; Abetz, C.; Li, X.; Wang, J.; Emrick, T.; Long, S.; Wang, Q.; Balazs, A.; Russell, T. P. Self-directed self-assembly of nanoparticle/copolymer mixtures. *Nature* **2005**, *434*, 55–59.
- (15) Yang, P.; Zhao, D.; Margolese, D. I.; Chmelka, B. F.; Stucky, G. D. Generalized syntheses of large-pore mesoporous metal oxides with semicrystalline frameworks. *Nature* **1998**, *396*, 152–155.
- (16) Warren, S. C.; Messina, L. C.; Slaughter, L. S.; Kamperman, M.; Zhou, Q.; Gruner, S. M.; DiSalvo, F. J.; Wiesner, U. Ordered Mesoporous Materials from Metal Nanoparticle—Block Copolymer Self-Assembly. *Science* **2008**, 320, 1748.
- (17) Stefik, M.; Mahajan, S.; Sai, H.; Epps, T. H.; Bates, F. S.; Gruner, S. M.; DiSalvo, F. J.; Wiesner, U. Ordered Three- and Five-ply Nanocomposites from ABC Block Terpolymer Microphase Separation with Niobia and Aluminosilicate Sols. *Chem. Mater.* **2009**, *21*, 5466–5473.
- (18) Rauda, I. E.; Buonsanti, R.; Saldarriaga-Lopez, L. C.; Benjauthrit, K.; Schelhas, L. T.; Stefik, M.; Augustyn, V.; Ko, J.; Dunn, B.; Wiesner, U.; Milliron, D. J.; Tolbert, S. H. General Method for the Synthesis of Hierarchical Nanocrystal-Based Mesoporous Materials. *ACS Nano* **2012**, *6*, 6386–6399.
- (19) Olson, M. A.; Coskun, A.; Klajn, R.; Fang, L.; Dey, S. K.; Browne, K. P.; Grzybowski, B. A.; Stoddart, J. F. Assembly of Polygonal Nanoparticle Clusters Directed by Reversible Noncovalent Bonding Interactions. *Nano Lett.* **2009**, *9*, 3185–3190.
- (20) Boal, A. K.; Ilhan, F.; DeRouchey, J. E.; Thurn-Albrecht, T.; Russell, T. P.; Rotello, V. M. Self-assembly of nanoparticles into structured spherical and network aggregates. *Nature* **2000**, *404*, 746–748.
- (21) Si, S.; Raula, M.; Paira, T. K.; Mandal, T. K. Reversible Self-Assembly of Carboxylated Peptide-Functionalized Gold Nanoparticles Driven by Metal-Ion Coordination. *ChemPhysChem* **2008**, *9*, 1578–1584
- (22) Fialkowski, M.; Bishop, K. J. M.; Klajn, R.; Smoukov, S. K.; Campbell, C. J.; Grzybowski, B. A. Principles and Implementations of Dissipative (Dynamic) Self-Assembly. *J. Phys. Chem. B* **2006**, *110*, 2482–2496.

- (23) Mirkin, C. A.; Letsinger, R. L.; Mucic, R. C.; Storhoff, J. J. A DNA-based method for rationally assembling nanoparticles into macroscopic materials. *Nature* **1996**, *382*, 607–609.
- (24) Mucic, R. C.; Storhoff, J. J.; Mirkin, C. A.; Letsinger, R. L. DNA-Directed Synthesis of Binary Nanoparticle Network Materials. *J. Am. Chem. Soc.* **1998**, *120*, 12674–12675.
- (25) Sánchez-Iglesias, A.; Grzelczak, M.; Altantzis, T.; Goris, B.; Pérez-Juste, J.; Bals, S.; Van Tendeloo, G.; Donaldson, S. H.; Chmelka, B. F.; Israelachvili, J. N.; Liz-Marzán, L. M. Hydrophobic Interactions Modulate Self-Assembly of Nanoparticles. *ACS Nano* **2012**, *6*, 11059–11065.
- (26) Percec, V.; Johansson, G.; Ungar, G.; Zhou, J. Fluorophobic Effect Induces the Self-Assembly of Semifluorinated Tapered Monodendrons Containing Crown Ethers into Supramolecular Columnar Dendrimers Which Exhibit a Homeotropic Hexagonal Columnar Liquid Crystalline Phase. J. Am. Chem. Soc. 1996, 118, 9855–9866.
- (27) Johansson, G.; Percec, V.; Ungar, G.; Zhou, J. P. Fluorophobic Effect in the Self-Assembly of Polymers and Model Compounds Containing Tapered Groups into Supramolecular Columns. *Macromolecules* **1996**, *29*, 646–660.
- (28) Darmanin, T.; Guittard, F. Fluorophobic Effect for Building up the Surface Morphology of Electrodeposited Substituted Conductive Polymers. *Langmuir* **2009**, *25*, 5463–5466.
- (29) Shimizu, S.; Kiuchi, T.; Pan, N. A "Teflon-Footed" Resorcinarene: A Hexameric Capsule in Fluorous Solvents and Fluorophobic Effects on Molecular Encapsulation. *Angew. Chem., Int. Ed.* **2007**, *46*, 6442–6445.
- (30) Shen, J.; Hogen-Esch, T. Block Copolymer-like Self-Assembly of Fluorocarbon End-Functionalized Polystyrene and Polybutylmethacrylate. *J. Am. Chem. Soc.* **2008**, *130*, 10866–10867.
- (31) Marsh, Z. M.; Blom, D. A.; Stefik, M. Tunable Fluorophobic Effect Determines Nanoparticle Dispersion in Homopolymers and Block Polymers. *Adv. Mater. Interfaces* **2020**, *7*, No. 1901691.
- (32) Groot, R. D.; Warren, P. B. Dissipative particle dynamics: Bridging the gap between atomistic and mesoscopic simulation. *J. Chem. Phys.* **1997**, *107*, 4423–4435.
- (33) Español, P.; Warren, P. B. Perspective: Dissipative particle dynamics. *J. Chem. Phys.* **2017**, *146*, No. 150901.
- (34) Español, P.; Warren, P. Statistical Mechanics of Dissipative Particle Dynamics. *Europhys. Lett.* **1995**, 30, 191.
- (35) Salib, I.; Yong, X.; Crabb, E. J.; Moellers, N. M.; McFarlin, G. T.; Kuksenok, O.; Balazs, A. C. Harnessing Fluid-Driven Vesicles To Pick Up and Drop Off Janus Particles. ACS Nano 2013, 7, 1224–1238
- (36) Chen, P.; Yang, Y.; Dong, B.; Huang, Z.; Zhu, G.; Cao, Y.; Yan, L.-T. Polymerization-Induced Interfacial Self-Assembly of Janus Nanoparticles in Block Copolymers: Reaction-Mediated Entropy Effects, Diffusion Dynamics, and Tailorable Micromechanical Behaviors. *Macromolecules* **2017**, *50*, 2078–2091.
- (37) Posocco, P.; Hassan, Y. M.; Barandiaran, I.; Kortaberria, G.; Pricl, S.; Fermeglia, M. Combined Mesoscale/Experimental Study of Selective Placement of Magnetic Nanoparticles in Diblock Copolymer Films via Solvent Vapor Annealing. *J. Phys. Chem. C* **2016**, *120*, 7403–7411.
- (38) Cai, C.; Wang, L.; Lin, J.; Zhang, X. Morphology Transformation of Hybrid Micelles Self-Assembled from Rod-Coil Block Copolymer and Nanoparticles. *Langmuir* **2012**, *28*, 4515–4524.
- (39) Yong, X. Modeling the Assembly of Polymer-Grafted Nanoparticles at Oil-Water Interfaces. *Langmuir* **2015**, *31*, 11458–11469.
- (40) Chen, S.; Yong, X. Janus Nanoparticles Enable Entropy-Driven Mixing of Bicomponent Hydrogels. *Langmuir* **2019**, *35*, 14840–14848.
- (41) Groot, R. D.; Rabone, K. L. Mesoscopic Simulation of Cell Membrane Damage, Morphology Change and Rupture by Nonionic Surfactants. *Biophys. J.* **2001**, *81*, 725–736.

- (42) Sirk, T. W.; Slizoberg, Y. R.; Brennan, J. K.; Lisal, M.; Andzelm, J. W. An enhanced entangled polymer model for dissipative particle dynamics. *J. Chem. Phys.* **2012**, *136*, No. 134903.
- (43) Palkar, V.; Kuksenok, O. Controlling Degradation and Erosion of Polymer Networks: Insights from Mesoscale Modeling. *J. Phys. Chem. B* **2022**, *126*, 336–346.
- (44) Plimpton, S. Fast Parallel Algorithms for Short-Range Molecular Dynamics. *J. Comput. Phys.* **1995**, *117*, 1–19.
- (45) LAMMPS. Molecular Dynamics Simulator. http://lammps.sandia.gov.
- (46) Humphrey, W.; Dalke, A.; Schulten, K. VMD: Visual molecular dynamics. *J. Mol. Graphics Model.* **1996**, *14*, 33–38.
- (47) Huang, J.; Luo, M.; Wang, Y. Dissipative Particle Dynamics Simulation on a Ternary System with Nanoparticles, Double-Hydrophilic Block Copolymers, and Solvent. *J. Phys. Chem. B* **2008**, 112, 6735–6741.
- (48) Langner, K. M.; Sevink, G. J. A. Mesoscale modeling of block copolymer nanocomposites. *Soft Matter* **2012**, *8*, 5102–5118.
- (49) Hpone Myint, K.; Brown, J. R.; Shim, A. R.; Wyslouzil, B. E.; Hall, L. M. Encapsulation of Nanoparticles During Polymer Micelle Formation: A Dissipative Particle Dynamics Study. *J. Phys. Chem. B* **2016**, *120*, 11582–11594.
- (50) Lee, M.-T.; Vishnyakov, A.; Neimark, A. V. Calculations of Critical Micelle Concentration by Dissipative Particle Dynamics Simulations: The Role of Chain Rigidity. *J. Phys. Chem. B* **2013**, *117*, 10304–10310.
- (51) Johnston, M. A.; Swope, W. C.; Jordan, K. E.; Warren, P. B.; Noro, M. G.; Bray, D. J.; Anderson, R. L. Toward a Standard Protocol for Micelle Simulation. *J. Phys. Chem. B* **2016**, *120*, 6337–6351.
- (52) Gumerov, R. A.; Potemkin, I. I. Computer simulations of comblike macromolecules with responsive diblock copolymer side chains. *Colloid Polym. Sci.* **2021**, 299, 407–418.
- (53) Lyubimov, I.; Wessels, M. G.; Jayaraman, A. Molecular Dynamics Simulation and PRISM Theory Study of Assembly in Solutions of Amphiphilic Bottlebrush Block Copolymers. *Macromolecules* **2018**, *51*, 7586–7599.
- (54) Yusa, S.-i.; Sakakibara, A.; Yamamoto, T.; Morishima, Y. Reversible pH-Induced Formation and Disruption of Unimolecular Micelles of an Amphiphilic Polyelectrolyte. *Macromolecules* **2002**, *35*, 5243–5249.
- (55) Costanzo, P. J.; Beyer, F. L. Thermally Driven Assembly of Nanoparticles in Polymer Matrices. *Macromolecules* **2007**, *40*, 3996–4001
- (56) Han, F.; Soeriyadi, A. H.; Vivekchand, S. R. C.; Gooding, J. J. Simple Method for Tuning the Optical Properties of Thermoresponsive Plasmonic Nanogels. *ACS Macro Lett.* **2016**, *5*, 626–630.
- (57) Yang, Y.; Serrano, L. A.; Guldin, S. A Versatile AuNP Synthetic Platform for Decoupled Control of Size and Surface Composition. *Langmuir* **2018**, *34*, 6820–6826.
- (58) Park, W. I.; Kim, J. M.; Jeong, J. W.; Jung, Y. S. Deep-Nanoscale Pattern Engineering by Immersion-Induced Self-Assembly. *ACS Nano* **2014**, *8*, 10009–10018.
- (59) Modi, A.; Bhaway, S. M.; Vogt, B. D.; Douglas, J. F.; Al-Enizi, A.; Elzatahry, A.; Sharma, A.; Karim, A. Direct Immersion Annealing of Thin Block Copolymer Films. *ACS Appl. Mater. Interfaces* **2015**, *7*, 21639–21645.
- (60) Flory, P. J. Thermodynamics of High Polymer Solutions. *J. Chem. Phys.* **1942**, *10*, 51–61.
- (61) Huggins, M. L. Solutions of long chain compounds. J. Chem. Phys. 1941, 9, 440.
- (62) Hostetler, M. J.; Green, S. J.; Stokes, J. J.; Murray, R. W. Monolayers in Three Dimensions: Synthesis and Electrochemistry of ω-Functionalized Alkanethiolate-Stabilized Gold Cluster Compounds. *J. Am. Chem. Soc.* **1996**, *118*, 4212–4213.
- (63) Marsh, Z. M.; Lantz, K. A.; Stefik, M. QCM detection of molecule—nanoparticle interactions for ligand shells of varying morphology. *Nanoscale* **2018**, *10*, 19107—19116.

- (64) Shah, P. S.; Holmes, J. D.; Doty, R. C.; Johnston, K. P.; Korgel, B. A. Steric Stabilization of Nanocrystals in Supercritical CO2 Using Fluorinated Ligands. *J. Am. Chem. Soc.* **2000**, *122*, 4245–4246.
- (65) Wang, X.; Dormidontova, E. E.; Lodge, T. P. The Order–Disorder Transition and the Disordered Micelle Regime for Poly(ethylenepropylene-b-dimethylsiloxane) Spheres. *Macromolecules* **2002**, *35*, 9687–9697.
- (66) Kuna, J. J.; Voïtchovsky, K.; Singh, C.; Jiang, H.; Mwenifumbo, S.; Ghorai, P. K.; Stevens, M. M.; Glotzer, S. C.; Stellacci, F. The effect of nanometre-scale structure on interfacial energy. *Nat. Mater.* **2009**, *8*, 837–842.
- (67) Pons-Siepermann, I. C.; Glotzer, S. C. Design of Patchy Particles Using Quaternary Self-Assembled Monolayers. *ACS Nano* **2012**, *6*, 3919–3924.
- (68) Tang, J.; Gao, K.; Ou, Q.; Fu, X.; Man, S.-Q.; Guo, J.; Liu, Y. Calculation extinction cross sections and molar attenuation coefficient of small gold nanoparticles and experimental observation of their UV—vis spectral properties. *Spectrochim. Acta, Part A* **2018**, *191*, 513—520.
- (69) Shi, H.; Zhang, L.; Cai, W. Preparation and optical absorption of gold nanoparticles within pores of mesoporous silica. *Mater. Res. Bull.* **2000**, 35, 1689–1695.
- (70) Hosoya, Y.; Suga, T.; Yanagawa, T.; Kurokawa, Y. Linear and nonlinear optical properties of sol-gel-derived Au nanometer-particle-doped alumina. *J. Appl. Phys.* **1997**, *81*, 1475–1480.

☐ Recommended by ACS

Photo-Cross-Linked Polymeric Dispersants of Comb-Shaped Benzophenone-Containing Poly(ether amine)

Yanchi Liu, Jin Li, et al.

APRIL 06, 2023

ACS APPLIED MATERIALS & INTERFACES

READ 🗹

Transparent Encryption of Nanostructured Photonic Patterns by Erasing the Structural Colors of Visible Patterns: Implications for Anti-Counterfeiting and Inform...

Ziqiang Tian, Shaoming Huang, et al.

SEPTEMBER 06, 2022

ACS APPLIED NANO MATERIALS

READ 🗹

Formation Mechanism of Flower-like Polyacrylonitrile Particles

Huaxin Gong, Zhenan Bao, et al.

SEPTEMBER 14, 2022

JOURNAL OF THE AMERICAN CHEMICAL SOCIETY

READ 🗹

${ m SiO_2}$ Nanoparticles in Polyurethane Colloidal Matrix for Color-Adjustable Photonic Coatings

Miao Tian, Pengxiang Si, et al.

AUGUST 09, 2022

ACS APPLIED NANO MATERIALS

READ 🗹

Get More Suggestions >